Oscillation of viscous drops with smoothed particle hydrodynamics

Hender López* and Leonardo Di G. Sigalotti†

Centro de Física, Instituto Venezolano de Investigaciones Científicas (IVIC), Apartado Postal 21827, Caracas 1020A, Venezuela

(Received 1 December 2005; revised manuscript received 21 February 2006; published 3 May 2006)

We investigate the nonlinear oscillations of heat-conductive, viscous, liquid drops in vacuum with zero gravity, using smoothed particle hydrodynamics (SPH). The liquid drops are modeled as a van der Waals fluid in two dimensions so that the models apply to flat, disklike drops. Attention is focused on small- to large-amplitude oscillations of drops that are released from a static elliptic shape. We find that for small-amplitude motions the combined dissipative effects of finite viscosity and heat conduction induce rapid decay of the oscillations after a few periods, while for large-amplitude motions wave damping is governed by the action of both viscous dissipation and surface tension forces. The transition from periodic to aperiodic decay at $\mathrm{Re}\sim 1$ as well as the quadratic decrease of the frequency with the initial aspect ratio at large Re are reproduced in good agreement with previous theoretical predictions and experimental results.

DOI: 10.1103/PhysRevE.73.051201 PACS number(s): 66.20.+d, 44.10.+i, 68.03.−g, 02.70.Ns

I. INTRODUCTION

Earlier studies of infinitesimal-amplitude oscillations of incompressible liquid drops about the spherical shape in vacuum take as their starting point the classical work by Lord Rayleigh [1] and Lord Kelvin [2]. The former author demonstrated that the normal-mode frequencies for an oscillating drop of density ρ and radius R, when the attainment of the spherical shape is governed by interfacial forces, are given by

$$\omega_n^2 = n(n-1)(n+2)\frac{\sigma}{\rho R^3}, \tag{1}$$

where σ is the surface tension and $n=2,3,\ldots$, stands for the mode number. The counterpart of Eq. (1) for two-dimensional drops oscillating about a circle is [1]

$$\omega_n^2 = n(n^2-1)\frac{\sigma}{\rho R^3}. \tag{2}$$

An oscillating, two-dimensional (planar) drop is physically represented by an infinitely long cylinder undergoing translationally symmetric deformations. The second author derived the corresponding analytical expressions for the frequency when the oscillating globe is held together by gravitational forces (see also Ref. [3]). Seventy years later, Chandrasekhar [4] provided an analytical solution to the damping of Kelvin modes by viscous dissipation. Later on, Reid [5] found that for arbitrary viscosity, the damping of a fluctuating drop in a tenuous gas is the same for gravity and surface tension. A number of other linear analyses has been performed in more recent times [6–8]. In particular, Prosperetti [8] studied the initial-value problem posed by the small-amplitude oscillations of free drops (i.e., drops surrounded by a dynamically inactive environment such as the vacuum or a low-density gas), gas bubbles, and drops in a host liquid. Using an alternative approach to the normal-mode technique, based on the use of Laplace transforms, he found that for small viscosities the motion consists of modulated damped oscillations, with varying frequency and damping parameter. In the case of free drops he found that initially the motion is that executed by a damped harmonic oscillator of natural frequency $\omega_n' = (\omega_n^2 - b_n^2)^{1/2}$, where

$$b_n = (n-1)(2n+1)\left(\frac{\sigma}{\rho R^3}\right)^{1/2}\frac{1}{\mathrm{Re}} \tag{3}$$

is the damping parameter, $\mathrm{Re}=(\rho\sigma R)^{1/2}/\eta$ is the Reynolds number, and η is the dynamic (shear) viscosity. Prosperetti's analysis also predicted a transition from periodic to aperiodic decay of the oscillations at low Re.

A second-order analytical solution for the oscillations of free inviscid drops, starting from moderate-amplitude deformations, was obtained by Tsamopoulos and Brown [9] by means of a Poincaré-Lindstedt expansion technique. Their analysis predicts a quadratic decrease of the oscillation frequency with the initial amplitude and the coupling between the linear modes, yielding the approximate expression for the frequency

$$\omega_n' = \omega_n[1 - \gamma c_n^2 + O(c_n^4)], \tag{4}$$

where c_n is the initial amplitude and $\gamma=0.638\,76$ for the fundamental $n=2$ mode.

Motivated by the importance of containerless processing technology in space, further studies of nonlinear drop oscillations have concentrated either on detailed numerical calculations or experiments with zero gravity. The first numerical simulations were performed by Foote [10], Alonso [11], and Lundgren and Mansour [12]. In particular, the latter authors used a boundary-integral method to calculate the large-amplitude motion of axisymmetric, slightly viscous ($\mathrm{Re}\geqslant 2000$) drops, finding that a small viscosity may have a relatively large effect on resonant-mode coupling. In addition, Patzek *et al.* [13] confirmed the predictions of Refs. [9,12] for large-amplitude oscillations of inviscid drops, using a Galerkin's weighted residual method. The effects of

*Electronic address: hlopez@ivic.ve
†Electronic address: lsigalot@cassini.ivic.ve

finite viscosity were first elucidated by Basaran [14], who performed Galerkin/finite-element-based calculations of nonlinear drop oscillations for $0.1 \leqslant \mathrm{Re} \leqslant 100$, focusing on drops released from a second spherical harmonic shape. An alternative approach for studying viscous drop oscillations with large amplitudes was presented by Becker *et al.* [15], who solved the Navier-Stokes equations using a method based on mode expansions. They found that frequency modulation and mode coupling are dominant, even in the case of small deformations. For large-amplitude oscillations, they obtained a general good agreement with the results of Refs. [12,14]. Mashayek and Ashgriz [16], using finite-element methods, calculated the nonlinear oscillations of drops with internal circulation, starting from second-, third-, fourth-, and fifth-mode spherical harmonic deformations. They showed that the internal circulation has significant effects on the frequency and damping rate during the first few periods of oscillation. Further calculations based on finite-element methods have recently been reported by Meradji *et al.* [17] for freely oscillating, viscous drops without internal circulation. While most of these calculations apply to axisymmetric oscillations of non-rotating, globular drops, Patzek *et al.* [18] investigated the nonlinear oscillations of two-dimensional, inviscid drops under the effects of rotation. They found that a major difference between the dynamics of nonrotating globular and rotating planar drops is in the type of surface waves that occur along the interface separating the drops from the surrounding medium. In particular, these waves are in the form of simple standing waves for the former drops, while the latter ones exhibit a complicated pattern of travelling and running capillary waves whose amplitudes grow with an increasing size of the rotation rate. Furthermore, the axisymmetric evolution of free liquid filaments, i.e., drops with very large initial aspect ratios of up to 1:60, have been calculated by Schulkes [19], and more recently, by Notz and Basaran [20], using finite-element methods. The latter authors have shown that filaments with $\mathrm{Re} \lesssim 10$ contract to their equilibrium spherical shapes without breaking into droplets, regardless of their initial elongation. When $\mathrm{Re} \gtrsim 10$, very long filaments pinch off daughter drops from their ends through the so-called end-pinching mechanism. For smaller elongations, the filaments undergo a sequence of complex oscillations that ultimately lead to breakup. Such oscillations, however, may also dissipate and lead to a final equilibrium spherical shape for even smaller initial elongations.

Experiments simulating zero gravity usually rely on some kind of levitation, which provides a freely floating drop, more or less spherical, and an optical detector to record the surface oscillations of the drop. For current liquids, acoustic levitation is the most common technique [21], while for liquid metals, electromagnetic levitation is the mostly used method [22]. The experimental observations of Trinh and Wang [23], based on acoustically levitated drops, confirmed the predictions of the linear theory for the frequency at small-amplitude oscillations. For large-amplitude oscillations, they found that the frequency decreases with the square of the initial amplitude in accordance with the second-order analysis of Ref. [9]. Experimental data of oscillating ethanol droplets in air, produced by the controlled breakup of a laminar jet discharging from a convergent nozzle, were obtained by Becker *et al.* [24]. They observed mode coupling and asymmetries in the oscillation amplitude of high-order modes only for drops with initial $n=2$ deformations larger than about 10% of their spherical radius. A new containerless method based on gas-film levitation of a liquid for measuring viscosity variations in fluctuating drops has been described by Popoular and Parayre [25]. For small-amplitude oscillations ($\lesssim$10% of the drop diameter) of levitated water-glycerol drops, they observed that both their geometrical aspect and the resonance profile are dissymmetric in general. Microgravity observations on board the Space Shuttle Columbia were reported by Wang *et al.* [26] and Apfel *et al.* [27]. In particular, the latter authors described the axisymmetric, quadrupole-mode oscillations of a surfactant-bearing water drop the size of a ping-pong ball over a complete period. Using a boundary-integral method they also reproduced the observed drop shapes.

Here we describe the results of numerical calculations of small- to large-amplitude oscillations of free liquid drops with $0.52 \lesssim \mathrm{Re} \lesssim 522$, using the method of smoothed particle hydrodynamics (SPH). The liquid is modeled as a van der Waals (vdW) fluid and the effects of heat conduction are included. The fluctuating drops all start from a perfectly elliptic shape, rather than a pure spherical harmonic deformation, in order to mimic the initial shape of the acoustically deformed water drop in the microgravity experiment of Ref. [27]. We limit ourselves to two-space dimensions so that the unperturbed drops are represented computationally by an infinitely thin, circular disk. Unlike Patzek *et al.* [18], we consider arbitrary viscosity and limit our analysis only to non-rotating drops. Apart from a few model calculations reported by Nugent and Posch [28], and more recently by Tartakovsky and Meakin [29], there is an almost complete lack of SPH calculations of oscillating liquid drops. We study the effects of varying the initial aspect ratio, the amount of viscosity, and the coefficient of thermal conductivity on the long-term evolution and compare with other theoretical and experimental results.

II. BASIC EQUATIONS AND SPH FORMULATION

The problem of a fluctuating liquid drop in a vacuum environment involves the solution of the equations of mass, momentum, and energy conservation for an incompressible fluid volume bounded by a free surface that separates the liquid from the outer vacuum. If viscous and heat-conduction effects are added, these equations become

$$\frac{d\rho}{dt} = -\rho \nabla \cdot \mathbf{v}, \tag{5}$$

$$\frac{d\mathbf{v}}{dt} = \frac{1}{\rho} \nabla \cdot \mathbb{T}, \tag{6}$$

$$\frac{dU}{dt} = \frac{1}{\rho} \mathbb{T} : \nabla \mathbf{v} - \frac{1}{\rho} \nabla \cdot \mathbf{q}, \tag{7}$$

where $\mathbf{v}$ is the velocity vector and U is the specific internal energy. Here $\mathbb{T}$ and $\mathbf{q}$ are the stress tensor and heat-flux vector, given by

$$\mathbb{T} = -p\mathbf{1} + \left[\eta(\nabla\mathbf{v} + \nabla\mathbf{v}^t) + \left(\zeta - \frac{2}{d}\eta\right)(\nabla\cdot\mathbf{v})\mathbf{1}\right], \quad (8)$$

and

$$\mathbf{q} = -\kappa\nabla T, \quad (9)$$

respectively, where the notation ^{t} in Eq. (8) means transposition. Here p is the isotropic pressure, T is the fluid temperature, ζ is the bulk viscosity, κ is the coefficient of heat conduction, d is the spatial dimension, and $\mathbf{1}$ is the unit tensor.

If the fluid is truly incompressible Eq. (5) becomes $\nabla\cdot\mathbf{v}=0$, while Eq. (6) reduces to the Navier-Stokes equations for an incompressible fluid. We restrict ourselves to two dimensions, $d=2$, and write Eqs. (5)–(9) in Cartesian coordinates so that $\mathbf{v}=(v_x,v_y)$, $\mathbf{q}=(q_x,q_y)$, and only the xx, xy, and yy components of the stress tensor $\mathbb{T}$ are retained. With this geometry, all variables are only functions of the (x,y) coordinates and time t. A spherical drop would then be represented by an infinitely thin, circular disk, with its oscillations about the spherical shape being quantified in terms of the deformations of the disk perimeter about its unperturbed circular shape.

The previous equations are closed by the mechanical and caloric equations of state for the pressure, p, and internal energy per unit mass, U, respectively. As in Ref. [28], we consider the vdW equations of state,

$$p = \frac{\rho\bar{k}_B T}{1-\bar{\beta}\rho} - \bar{\alpha}\rho^2, \quad (10)$$

and

$$U = \frac{\xi}{2}\bar{k}_B T - \bar{\alpha}\rho, \quad (11)$$

which are obtained in the mean-field limit for the free energy density of a system of hard particles of radius r_0. Here $\bar{k}_B = k_B/m$, $\bar{\alpha}=\alpha/m^2$, $\bar{\beta}=\beta/m$, and ξ is the number of degrees of freedom for the particles, where k_B is the Boltzmann's constant, α is the cohesive action, β is a constant parameter due to the finite size of the particles, and m is the mass particle. In two dimensions, $\beta=2\pi r_0^2$ and $\xi=2$.

Standard SPH, coupled with an adaptive density kernel estimation procedure as described by Silverman [30], is used to solve Eqs. (5)–(7). A detailed account of the method can be found in Ref. [31], where it has been applied to incompressible flow in a pipe, and in Ref. [32], where it has been used to model compressible flows with strong shocks. Here we shall only provide a brief description of the method. As it is almost always used in SPH simulations, the continuity equation (5) is replaced by an interpolant summation for the density at each point. For particle i, this summation is

$$\rho_i = \sum_{j=1}^{N} m_j W_{ij}, \quad (12)$$

where $W_{ij}=W(|\mathbf{x}_i-\mathbf{x}_j|,h)$ is the kernel interpolation function and h is a measure of its width. The summation includes the contribution of particle i itself and conserves the total mass exactly. In principle, it is taken over all sample particles though in practice only the nearest neighbors contribute because of the finite range of the kernel. Following Bonet and Lok [33], the use of Eq. (12) demands that the SPH replacements for the momentum and thermal energy equations must be written in symmetrized form in order to preserve variational consistency. We use symmetrized forms of the particle equations of motion and thermal energy that contain the full Newtonian stress tensor $\mathbb{T}$ and heat-flux vector $\mathbf{q}$ (see Ref. [28]),

$$\frac{d\mathbf{v}_i}{dt} = \sum_{j=1}^{N} m_j\left(\frac{\mathbb{T}_i}{\rho_i^2} + \frac{\mathbb{T}_j}{\rho_j^2}\right)\cdot\nabla_i W_{ij}, \quad (13)$$

$$\frac{dU_i}{dt} = \frac{1}{2}\sum_{j=1}^{N} m_j\left(\frac{\mathbb{T}_i}{\rho_i^2} + \frac{\mathbb{T}_j}{\rho_j^2}\right):(\mathbf{v}_j-\mathbf{v}_i)\nabla_i W_{ij} - \sum_{j=1}^{N} m_j\left(\frac{\mathbf{q}_i}{\rho_i^2} + \frac{\mathbf{q}_j}{\rho_j^2}\right)\cdot\nabla_i W_{ij}, \quad (14)$$

where the colon in the second equation indicates a double dot product. The velocity gradients and the velocity divergence involved in the definition of the stress tensor (8) are evaluated by means of the SPH expansions,

$$(\nabla\mathbf{v})_i = \frac{1}{\rho_i}\sum_{j=1}^{N} m_j(\mathbf{v}_j-\mathbf{v}_i)\nabla_i W_{ij}, \quad (15)$$

and

$$(\nabla\cdot\mathbf{v})_i = \frac{1}{\rho_i}\sum_{j=1}^{N} m_j(\mathbf{v}_j-\mathbf{v}_i)\cdot\nabla_i W_{ij}, \quad (16)$$

respectively. An expansion similar to Eq. (15) is used to evaluate the temperature gradient needed for the heat flux in Eq. (9). The position of particle i is determined by means of the equation

$$\frac{d\mathbf{x}_i}{dt} = \mathbf{v}_i, \quad (17)$$

which must be solved simultaneously with Eqs. (12)–(14).

Equations (13) and (14) are suitable for treating compressible fluids with arbitrary shear and bulk viscosities. However, it has been shown in Ref. [31] that if they are combined with the pressure-gradient correction proposed by Morris *et al.* [34], they are also suitable for treating incompressible flows accurately. Linearization of the vdW equations of state (10) and (11) gives the pressure variation in terms of the density and temperature variations,

$$\delta p = c_s^2\,\delta\rho + \frac{\bar{k}_B\rho}{1-\bar{\beta}\rho}\delta T, \quad (18)$$

where

$$c_s = \left(\frac{\bar{k}_B T}{(1-\bar{\beta}\rho)^2} - 2\bar{\alpha}\rho \right)^{1/2}, \tag{19}$$

is the sound speed. It can be shown that for relatively large κ, as used in this work, temperature fluctuations are efficiently eradicated by the high thermal conductivity and/or temperature gradients. Thus $\delta T \ll 1$ and so $\delta p \approx c_s^2\, \delta\rho$, with a good approximation. Incompressibility (i.e., $\delta p \ll 1$) would then require having $\delta\rho \ll 1$. In general, incompressible fluids have a speed of sound much larger than the speed v of the bulk flow, implying that the relative fluctuations in density $\delta\rho/\rho$, which are proportional to the square of the Mach number, $M = v/c_s$, are very small [35]. Since this is often the case for the damped oscillations of a liquid drop, we find that the flow incompressibility is well reproduced by the above SPH formulation, with no need of implementing the pressure-gradient corrections suggested by Morris *et al.* [34].

The accuracy and stability of standard SPH is significantly improved when the smoothing is performed adaptively by means of a density kernel estimation similar to that described by Silverman [30]. The idea behind this class of estimates is to construct a collection of local kernels centered at the positions of the particles in order to allow the bandwidth, h, to vary from point to point. In order to do so, we first compute an initial (or pilot) density estimate, $\hat{\rho}_i$, using Eq. (12) written as

$$\hat{\rho}_i = \sum_{j=1}^{N} m_j W(|\mathbf{x}_i - \mathbf{x}_j|, h_{i,0}), \tag{20}$$

where $h_{i,0}$ can be defined as some dilation factor of the initial interparticle separation. Local bandwidth factors, say λ_i, are next constructed according to the relation

$$\lambda_i = k\left(\frac{\hat{\rho}_i}{\bar{g}} \right)^{-\varepsilon}, \tag{21}$$

where k is a constant scaling factor of the order of unity, ε is the sensitivity parameter defined in the interval $0 \leqslant \varepsilon \leqslant 1$, and $\bar{g}$ is the geometric mean of the pilot estimates, calculated as

$$\log \bar{g} = \frac{1}{N} \sum_{i=1}^{N} \log \hat{\rho}_i. \tag{22}$$

As a final step, the adaptive estimator is obtained by defining the width of the kernel at the position of particle i as $h_i = \lambda_i h_{i,0}$ and by recalculating the density using Eq. (20) with $h_{i,0}$ replaced by h_i. When $\varepsilon \to 1$, the λ_i's become more sensitive to variations in the pilot density distribution, implying a greater difference of the h_i's in different parts of the sample. On the contrary, $\varepsilon = 0$ leads to the usual kernel approach, provided that $k = 1$ in Eq. (21). This method combines intrinsic features of both the kernel and nearest neighbor approaches so that the amount of smoothing applied to the data is effectively minimized. This improves the stability of standard SPH in the vecinity of strong shocks [32] and removes the tensile instability for a wide range of the parameters k and ε [36]. In order to improve the conservation of linear momentum, angular momentum, and total energy, the kernel estimate is symmetrized with respect to particle pairs by replacing h_i by the mean $h_{ij} = (h_i + h_j)/2$. In this way, the final kernel employed in Eqs. (12)–(14) is $W_{ij} = W(|\mathbf{x}_i - \mathbf{x}_j|, h_{ij})$. In this work, we adopt the quartic spline kernel of Lucy [37]. With this kernel only nearest particles within a circular zone of influence of radius h_i around particle i contribute to the SPH summations in Eqs. (12)–(14).

A predictor-corrector leapfrog integrator is used to advance the position, velocity, and thermal energy of the particles through a complete time step, $\Delta t = t^{l+1} - t^l$. In the predictor stage, quantities are first evolved to the intermediate time, $t^{l+1/2}$, using the sequence

$$\mathbf{x}_i^{l+1/2} = \mathbf{x}_i^{l-1/2} + \Delta t\, \mathbf{v}_i^l,$$

$$\mathbf{v}_i^{l+1/2} = \mathbf{v}_i^l + \frac{1}{2}\Delta t \left(\frac{d\mathbf{v}}{dt} \right)_i^l,$$

$$U_i^{l+1/2} = U_i^l + \frac{1}{2}\Delta t \left(\frac{dU}{dt} \right)_i^l. \tag{23}$$

Intermediate values of the density and temperature are next determined from $\mathbf{x}_i^{l+1/2}$ and $U_i^{l+1/2}$ using Eqs. (12) and (11), respectively. With these updates, the time-centered pressure is obtained from Eq. (10). The acceleration, $(d\mathbf{v}/dt)_i^{l+1/2}$, and the time rate of change of the thermal energy, $(dU/dt)_i^{l+1/2}$, are next calculated for use in the corrector step,

$$\mathbf{x}_i^{l+1} = \mathbf{x}_i^l + \Delta t\, \mathbf{v}_i^{l+1/2},$$

$$\mathbf{v}_i^{l+1} = \mathbf{v}_i^l + \Delta t \left(\frac{d\mathbf{v}}{dt} \right)_i^{l+1/2},$$

$$U_i^{l+1} = U_i^l + \Delta t \left(\frac{dU}{dt} \right)_i^{l+1/2}, \tag{24}$$

from which final updates of the density, temperature, and pressure are computed. To maintain numerical stability with the above explicit scheme, the time step must be limited by the CFL condition (see Ref. [38]). However, for the calculations of this paper a constant time step ($\Delta t = 0.005$) was enough to guarantee numerical stability. Although the present calculations are constrained to two-space dimensions, the extension of the method to handle full three-dimensional drops is straightforward.

III. UNPERTURBED DROP MODEL

The oscillating drop models all start from an elliptic shape obtained by deforming a stable circular drop, as shown in Fig. 1. The circular drop is constructed numerically by starting the calculation with a square-cell array of 900 SPH particles of equal mass. Initially all particles are at rest with a dimensionless separation distance $\Delta s = 0.75$ along the x and y axes. We adopt the same vdW parameters of Nugent and Posch [28], namely $m_i = m = 1$, $\bar{\alpha} = 2$, $\bar{\beta} = 0.5$, and $\bar{k}_B = 1$ in reduced units. This choice leads to a vdW fluid whose critical point occurs for $\rho_{cr} = 2/3$, $p_{cr} = 8/27$, and $T_{cr} = 32/27$ [35].

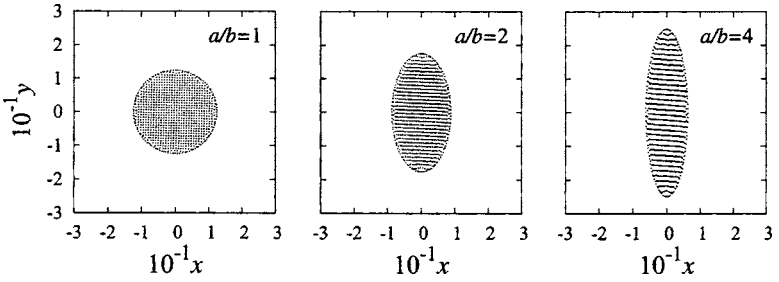

FIG. 1. Reference circular drop in equilibrium (*left panel*) and deformed elliptic drops with prolate aspect ratios $a/b=2$ (*middle panel*), and $a/b=4$ (*right panel*) after homogeneous flattening by pure shear strain.

The initial density and temperature are chosen such that they obey the constraints $\rho_0 < 1/\bar{\beta}$ and $\bar{k}_B T_0 > 2\bar{\alpha}\rho_0(1-\bar{\beta}\rho_0)^2$ for thermodynamic stability. These inequalities are satisfied by assigning a uniform temperature $T_0=0.2$ to each particle and by determining the density from Eq. (12) with $h_{i,0}=3\,\Delta s$. We further choose $\eta=1$, $\zeta=1$, and $\kappa=5$ in reduced units along with the adaptive kernel estimation parameters $k=0.9$ and $\varepsilon=0.6$. With a subcritical temperature of 0.2, a stable circular drop of smoothed central density $\rho(0)\approx 1.764$, pressure $p(0)\approx 0.156$, temperature $T(0)\approx 0.42$, and radius $R\approx 12.27$, with no external atmosphere, is formed, as displayed in the left panel of Fig. 1. Using the Laplace formula the surface tension is $\sigma=p(0)R\approx 1.91$. Nugent and Posch [28] obtained $\sigma=4.2$ for a similar stable circular drop. Compared to our drop model, their higher value of the surface tension is primarily due to their circular drop having a comparatively larger radius ($R=22.2$), which is about twice the radius of the circular drop shown in Fig. 1. The evolution of the kinetic (K) and thermal (U) energies for this drop is displayed in Fig. 2. At $t=600$, when the calculation is terminated, $K\to 0$ and U tends to a negative constant value, implying that the drop is in thermomechanical equilibrium.

Due to the crippling deficiency of particles at the borders of the initial square array, the use of Eq. (12) produces densities there that are lower than the uniform value carried by the interior particles. As a result, a smooth density profile, rather than a discontinuous jump, forms at the drop boundary, which allows the surface evolution to proceed stably without any particular treatment of the outer boundary. As in Nugent and Posch [28], we use the attractive central forces, due to the cohesive term in Eq. (10), to handle surface tension effects. In this method, the cohesive contributions to the acceleration and heating, namely

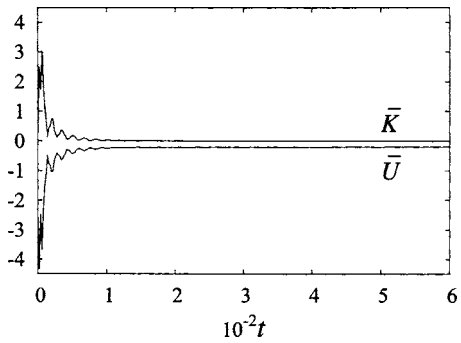

FIG. 2. Time variation of the kinetic (K) and thermal (U) energies during the evolution, leading to the equilibrium, circular drop shown in Fig. 1. For convenience, $\bar{K}=K/10$ and $\bar{U}=(U+2640)/10$ are plotted instead of K and U. All quantities are in reduced units.

$$\frac{d\mathbf{v}_i}{dt} = 2\bar{\alpha}\sum_{j=1}^{N} m_j \nabla_i W_{ij}^H, \tag{25}$$

and

$$\frac{dU_i}{dt} = 2\bar{\alpha}\sum_{j=1}^{N} m_j(\mathbf{v}_j - \mathbf{v}_i)\cdot\nabla_i W_{ij}^H, \tag{26}$$

respectively, are evaluated separately from all other SPH terms. Here $W_{ij}^H = W(|\mathbf{x}_i - \mathbf{x}_j|, H)$, where $H \geqslant 2h_0$. Equation (25) strongly resembles that used by Morris [38] to estimate the surface normals for calculating interfacial curvatures with SPH using the continuum-surface-force (CSF) method. The above choice of H is then determined by the same considerations that led to improved interfacial stability with the CSF method [38]. The forces represented by Eq. (25) largely cancel within the drop, except for a small strip H around the drop surface, where the particles are accelerated in the direction of the inward surface normal. This translates into a net surface tension due to the local curvature.

IV. OSCILLATING VISCOUS DROPS

We consider the oscillatory motion of drops that are released from an initial (static) elliptic deformation. The reference circular drop is deformed into an elliptic shape by homogeneous flattening under pure shear strain [39]. This involves an area-preserving coordinate transformation, given by

$$\begin{pmatrix} x' \\ y' \end{pmatrix} = \begin{pmatrix} (1+\epsilon)^{-1} & 0 \\ 0 & 1+\epsilon \end{pmatrix}\begin{pmatrix} x \\ y \end{pmatrix}, \tag{27}$$

where the parameter ϵ is the elongation and $1+\epsilon$ is the stretch. The above transformation will convert the circle into an ellipse whose semimajor axis a is aligned with the y axis, as shown in Fig. 1. As the drop is deformed into an ellipse, the interparticle spacing stretches in the x direction and expands in the y direction. For strong flattening (i.e., large prolate aspect ratios), the interparticle separation in the x direction becomes much smaller than along the y direction, and so the isotropic (circular) smoothing length can become significantly larger than the mean interparticle spacing along the direction of flattening, while becoming significantly smaller than the mean interparticle spacing in the transverse direction (of maximum drop elongation). The former mismatch reduces the spatial resolving power of the method, while the latter causes neighboring particles to lose contact, and may lead to unstable behavior. A number of test calculations with

increasing drop flattening shows that with a circular smoothing length the method can only follow the oscillations of drops with initial aspect ratios $a/b \lesssim 5$. For larger aspect ratios, it is necessary to revert to an anisotropic smoothing kernel that adjusts so as to follow the changes of the local mean interparticle spacing with direction around each fluid element [40]. Hence, for very elongated drops the smoothing kernels would no longer be circular but rather elliptical, with their semimajor axes aligned with that of the main drop. Here we shall consider only initial drop deformations with $a/b \leqslant 4$, and defer both the implementation of the above refinements and the evolution of liquid filaments for a next paper. Returning to Fig. 1, the semimajor and semiminor axes of the elliptical drops obey the relations $a=(1+\epsilon)R$ and $b=R/(1+\epsilon)$, respectively, where R is the radius of the unperturbed drop. The initial shape of the drop is therefore given by

$$f(\phi,0) = \left(\frac{\cos^2\phi}{a^2} + \frac{\sin^2\phi}{b^2}\right)^{-1/2}, \tag{28}$$

for $0 \leqslant \phi < 2\pi$.

The models are parametrized by the Reynolds number Re, the initial prolate aspect ratio a/b, and the Péclet number $\mathrm{Pe}=c_p(\rho\sigma R)^{1/2}/\kappa$, where c_p is the specific heat at constant pressure. The latter number is a measure of the importance of heat conduction. The effects of varying the initial aspect ratio from $a/b=1.2$ to 4 are studied for drops with low Reynolds number in the range between $\mathrm{Re}\approx 6.27$ and ≈ 62.69. Two independent sequences of models with fixed a/b (=1.5 and 3) each are also defined for drops with $0.52 \lesssim \mathrm{Re} \lesssim 522$. Finally, the coefficient of heat conduction is varied in the range $1 \leqslant \kappa \leqslant 10$ for drops with $\mathrm{Re}\approx 62.69$ and aspect ratios $a/b=1.5$ and 3, providing two additional sequences of models with $0.015 \lesssim \mathrm{Pe} \lesssim 0.15$. In all cases, the coefficient of bulk viscosity was taken to be $\zeta=0.1$. Due to the liquid incompressibility, test calculations with varied ζ and keeping all other parameters the same have produced almost undistinguishable results.

The surface energy E_S per unit length, or "line" energy of the elliptic drop, measured relative to a circular drop having the same area, is given by

$$E_S = \frac{1}{2\pi R}\int_0^{2\pi} (f^2 + f_\phi^2)^{1/2}\, d\phi - 1, \tag{29}$$

where f_ϕ is the ϕ derivative of the shape function (28). In the previous equation, energy is measured in units of $2\pi R\sigma$, which is the surface energy per unit length of an infinitely extended cylinder of radius R. Figure 3 depicts the variation of the line energy with the initial aspect ratio over a wide range of elliptic deformations. During its oscillations, the drop may pass through transient contours that will not fit a perfect ellipse due to nonlinear coupling of the oscillation modes. It is therefore necessary to track the drop contour numerically during its deformation. With SPH, this is done in a very straightforward manner by identifying the boundary particles at each time step. Using their Cartesian coordinates (x_b, y_b), defined with respect to the drop's center of mass, we may then calculate their azimuthal angles, $\phi_b=\tan^{-1}(x_b/y_b)$, measured with respect to the positive y axis ($\phi=0$), and their radial distances, $r_b=y_b\cos\phi_b$, from the center of mass. The radii of all boundary particles then provide a discrete set of values that define the shape function, f_b.

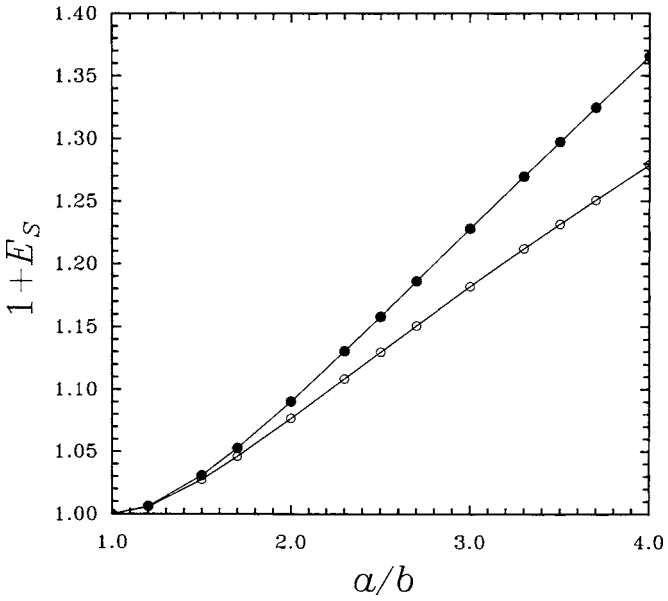

FIG. 3. Surface energy per unit length, E_S, for the initial elliptic drop shapes (solid line with filled dots) as a function of the maximum prolate aspect ratio, a/b. Also shown are the corresponding surface energies of initially prolate spheroidal drops (solid line with open circles).

The time resolved evolution of a highly viscous ($\mathrm{Re}\approx 6.27$) drop released from an elliptic $a/b=4$ deformation is shown in Fig. 4 during its first period of oscillation. Expressed in units of the critical time $t_c=(\rho R^3/\sigma)^{1/2}$, the first period ($t=109$) is $\tau_1 \approx 2.7065$, while the aspect ratio at that time is $a/b \approx 1.2$. The aspect ratio decays further to ≈ 1.049 at the end of the second period ($\tau_2 \approx 4.7427$, in units of t_c). Thereafter the drop undergoes very small oscillations about an approximate circular shape. For comparison, Fig. 5 shows a sequence of shapes that result when a similar elliptic drop is released at $\mathrm{Re}\approx 62.69$. In this case, the drop completes its first oscillation period after a longer time $t/t_c \approx 2.905$ ($t=115$), achieving a much larger aspect ratio $a/b \approx 2.3$. The shapes depicted in Fig. 5 strongly resemble those found by Basaran [14] at $\mathrm{Re}=100$ for a drop released from a prolate spheroidal shape with $a/b=3$. The re-entrant (concave) shape visible in Fig. 5 at $t=57$ (or $t/t_c=1.4153$) is typical of real oscillating drops released from prolate/oblate shapes at moderate and high Re at the time of maximum oblateness/prolateness. This feature has also been observed in microgravity experiments of oscillating water drops at $\mathrm{Re}=600$ [27]. Linear theory predicts that the drop shape should also be re-entrant at the end of each period. However, the asymptotic results of Tsamopoulos and Brown [9] and the finite-element calculations of Basaran [14] have shown that this feature may be absent for large-amplitude oscillations, in good agreement with the result of Fig. 5 at $t=115$.

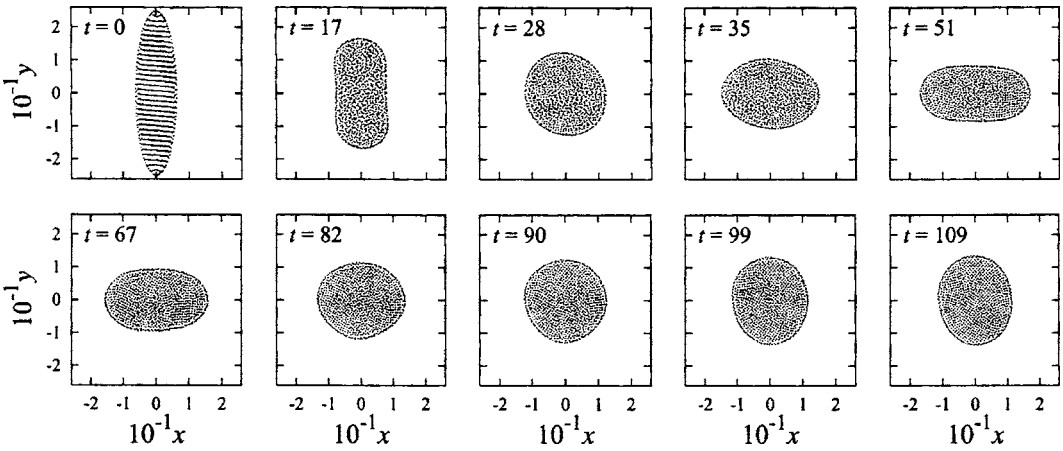

FIG. 4. Shapes during the first oscillation period that result when a liquid drop is released from an elliptic deformation with aspect ratio $a/b=4$ ($t=0$) at Re$\approx$6.27. In each panel the time is shown in reduced units.

The internal flow field is depicted in Fig. 6 for the oscillating drop shown in the sequence of Fig. 5. In order to compare with the photographic patterns of Trinh and Wang [23] (see their Fig. 12), showing the internal flow field of a silicon oil drop oscillating in the $n=2$ mode, we have chosen four distinct times all corresponding to the stage toward the point of maximum flatness ($t=57$ in Fig. 5). At $t=18$, when the elliptic drop is contracting along its semimajor axis, a counterflow develops, which at this time is mainly limited to the end caps of the still prolate drop. As the drop contracts further and passes through an approximate circular shape, the counterflow transforms into a nearly steady drifting motion ($t=25$). At this time, the drift involves mostly the outer parts of the drop and causes an outflow directed along the x axis. As the drop deforms into an oblate shape, the steady drift spreads into the inner drop regions ($t=35$). Note, however, that the center of the drop remains nearly motionless. A very similar behavior was observed in the experiments of Trinh and Wang [23]. In particular, the patterns shown in the upper-right and bottom-left panels of Fig. 6 reproduce fairly well the flow pictures in their Fig. 12, except for the development of a fourfold circulatory flow pattern on each side of the intersecting coordinate axes. However, they interpreted the appearance of internal circulation as probably caused by the asymmetry in the acoustic field. We also note that the internal flow remains subsonic as the maximum velocities are always much smaller than the speed of sound $c_s\approx 4.81$. At $t=57$, when the drop reaches its maximum flatness most of the undamped internal kinetic energy goes into surface energy.

Figures 7 and 8 compare the damped oscillations of a drop at Re$\approx$6.27 and $\approx$62.69, respectively, when the initial deformation is varied from $a/b=1.2$ to 4. The damping is mostly due to viscous dissipation and, to some extent, to the finite heat conductivity ($\kappa=5$, Pe$\approx$0.029). A value of κ this large was used to obtain fast temperature adjustment and reduce density fluctuations in the drop. As was shown by Nugent and Posch [28], the intrinsic viscosity that is inherent to particle systems may also contribute to damping, even for vanishing η. However, a test with $\eta=0$ and $\kappa=0$ confirms that the damping rate due to this latter effect is effectively much slower than that due to either finite physical viscosity or heat conductivity. As expected, wave damping is stronger for Re$\approx$6.27 than for Re$\approx$62.69. When the initial aspect ratio is increased for fixed Re, the amplitude of the oscillations increases and the first period is attained at progressively longer times. As we shall see later, in the present disklike

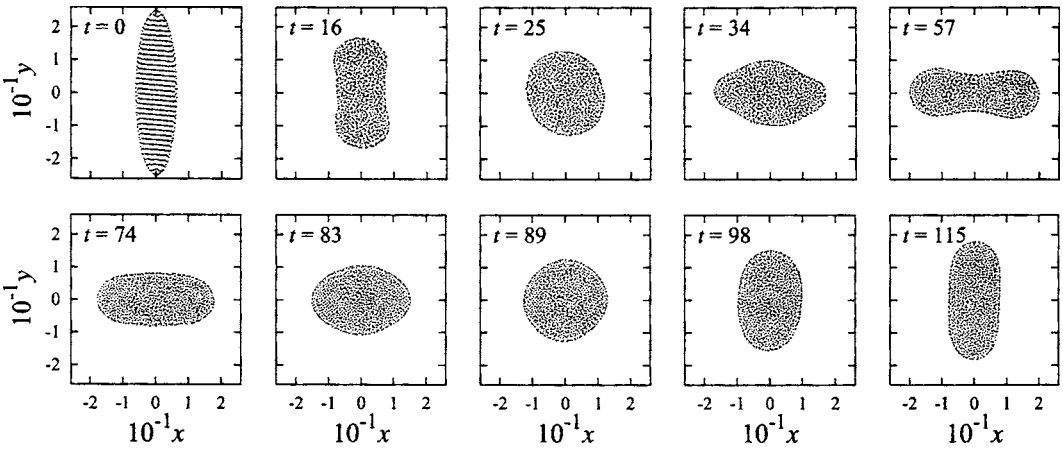

FIG. 5. Shapes during the first oscillation period that result when a liquid drop is released from an elliptic deformation with aspect ratio $a/b=4$ ($t=0$) at Re$\approx$62.69. In each panel the time is shown in reduced units.

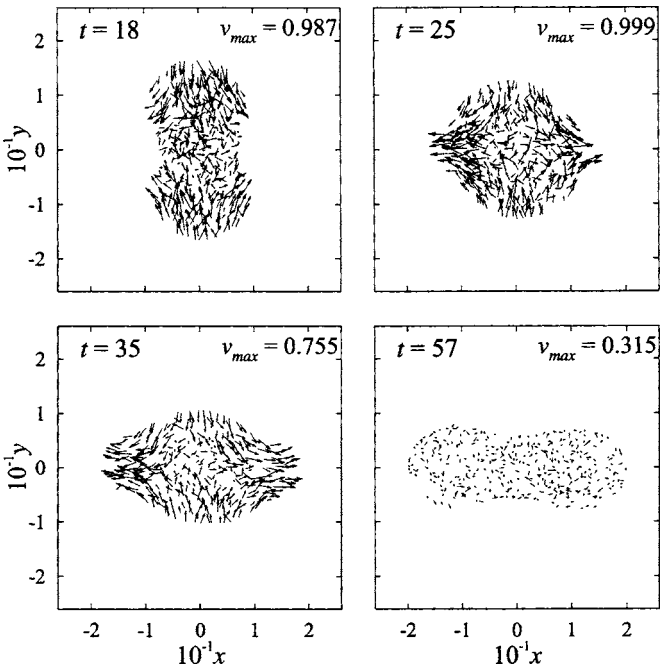

FIG. 6. Internal velocity field at four distinct times during the stage towards the point of maximum flatness for the oscillating drop shown in the sequence of Fig. 5. The time and the maximum velocity are given in reduced units. Only 40% of the actual number of particles is shown for clarity.

drop models the damping effects of heat conduction are much stronger for small-amplitude motions. For large-amplitude oscillations surface tension forces are likely to be more important. This can be better understood with the help of Fig. 3, where the line energy of an elliptic drop is compared with the surface energy of a prolate spheroidal drop for various aspect ratios. We see that for small deformations ($a/b \leqslant 2$) there is not much difference between these energies. However, at larger aspect ratios the line energy of an infinitely flattened drop becomes progressively greater than the surface energy of a prolate spheroidal drop, implying that a greater force is required to deform an ellipse into large aspect ratios. This may explain why the oscillations shown in Figs. 7 and 8 for initial aspect ratios $a/b \geqslant 3$ get damped out after a fewer number of periods compared to those experienced by similarly deformed elongated spheroidal drops [14,17].

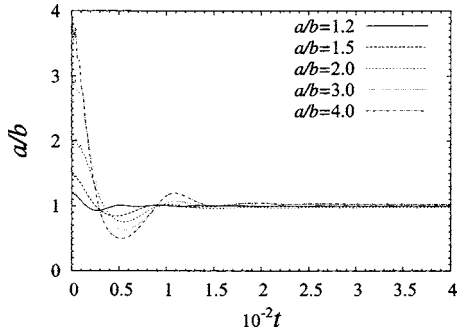

FIG. 7. Variation of the drop aspect ratio, a/b, with time for different initial elliptic drop deformations at Re$\approx$6.27. The time is given in reduced units.

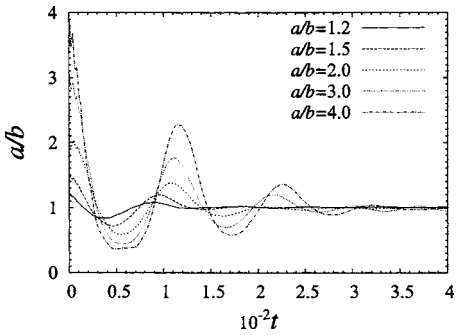

FIG. 8. Variation of the drop aspect ratio, a/b, with time for different initial elliptic drop deformations at Re$\approx$62.69. The time is given in reduced units.

Decomposition of the drop shape into its linear modes is accomplished by expanding the shape function, $f(\phi,t)$, in terms of the cosine Fourier series,

$$f(\phi,t) - 1 = \frac{c_0(t)}{2} + \sum_{n=1}^{\infty} c_n(t)\cos(n\phi), \tag{30}$$

where the coefficients $c_n(t)$ are the mode amplitudes, which can be expressed as cosine integrals of $f(\phi,t)-1$ over ϕ, after use of the orthogonality condition of the cosine functions. The integrals are here approximated by means of Riemann summations over all boundary particles, using the discrete numerical values f_b-1. In particular, Fig. 9 shows the calculated amplitudes of the first leading Fourier modes versus time for the drop shape sequence of Fig. 5 (the dot-dashed wave in Fig. 8). We see that the primary $n=2$ mode dominates the other modes. For oscillation amplitudes this large the deformation shows clear signs of other harmonics in contrast to the $a/b \leqslant 2$ cases, where higher-order modes, with the exception of the $n=4$ and perhaps $n=6$ modes, keep essentially at a level of pure noise. This feature agrees with the results of previous calculations of small-amplitude drop oscillations with arbitrary viscosity. Because of viscous dissipation the frequency of the primary $n=2$ mode is shifted with respect to its natural (Rayleigh) frequency, $\omega_2 t_c = \sqrt{6}$. The zeroth- and higher-order modes are excited by nonlinear coupling with the second mode. In particular, the linear frequency of the fourth mode, $\omega_4 t_c = 2\sqrt{15}$, is about three times larger than that of the second mode. A close inspection of Fig. 9 shows that the first minimum of the $n=4$ amplitude appears at about one-third of the time at which the minimum of the $n=2$ amplitude occurs. Due to dissipational effects, the frequency of the $n=4$ mode also shifts and becomes twice that of the primary $n=2$ mode. Also, the zeroth mode is excited at twice the frequency of the second mode, while the sixth and the eighth modes are excited at approximately twice the frequency of the fourth mode. In contrast, linear theory predicts that the natural frequencies of the $n=6$ and $n=8$ modes are about 1.87 and 2.90 times higher than that of the $n=4$ oscillation mode. Small asymmetries are present in the transient shapes displayed in Figs. 4 and 5 due to the excitation of odd modes (essentially the $n=3$ mode). Since the amplitudes of these modes always keep at a low level

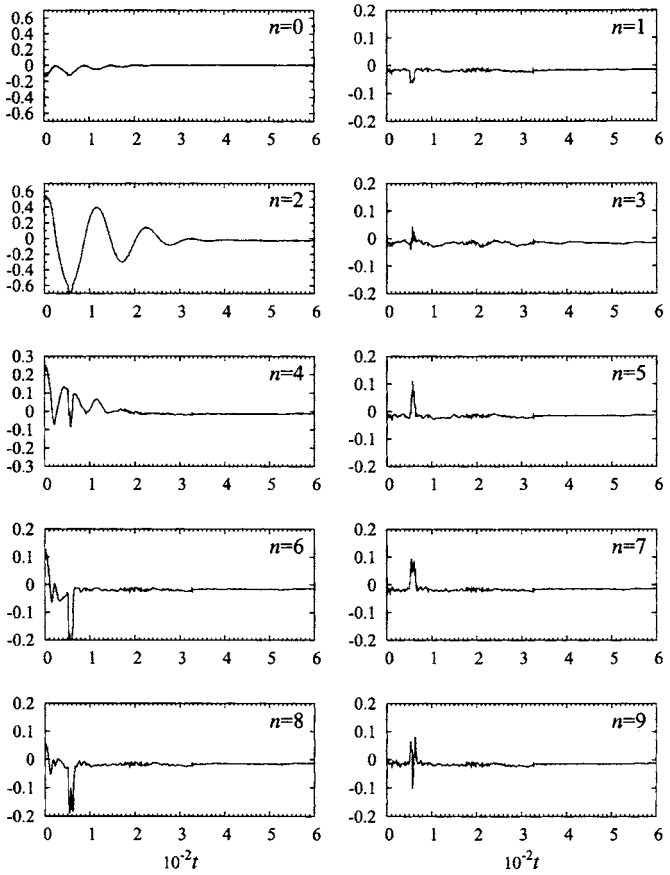

FIG. 9. Temporal variation of the amplitudes, c_n, of the first nine Fourier modes for the shape sequence shown in Fig. 5. The amplitudes are expressed in terms of the radius R of the unperturbed circular drop and the time is given in reduced units.

(see Fig. 9), only small asymmetric drop surface displacements occur during the first oscillation period. Compared to most previous grid-based calculations, surface asymmetries are expected with SPH because the internal motion is not constrained by symmetry conditions needed to maintain regularity of the velocity field at singular points (or regions) of a specific coordinate system. In passing, we note that nonzero odd-mode amplitudes were also reported by Patzek *et al.* [18] in their Galerkin/finite-element, two-dimensional calculations of the finite amplitude oscillations of a nonrotating, inviscid drop starting from an $n=4$ initial deformation (their Figs. 23 and 24). The time at which the downward (for $n=1$, 6, and 8 modes) and upward (odd modes with $n \geqslant 3$) spikes occur in Fig. 9 coincides with the time of the first minimum of the $n=2$ mode amplitude, suggesting a kind of resonant interaction between these modes and the second one. While this feature is typical of large-amplitude oscillations at high Re, similar amplitude variations to those shown in Fig. 9 were obtained for all other oscillating drops. Moreover, it is clear that the effect of viscosity is to damp out the higher modes faster than the lower ones, a feature that is also in accordance with the results of previous calculations of oscillating axisymmetric drops [14,16].

The effects of increasing the strength of the viscous forces over the inertial ones for large-amplitude ($a/b=3$) drop oscillations are shown in Fig. 10. We may see that the calculations predict a change in the regime of the oscillations from underdamped (periodic) when $5 \lesssim \mathrm{Re} \lesssim 522$, to critically damped when $\mathrm{Re}=1$, corresponding to a fast aperiodic return to the circular rest state, and then to overdamped when $\mathrm{Re} \approx 0.5$, corresponding to a slower aperiodic decay mode that dominates the motion at large times [6,8]. For infinitesimal-amplitude oscillations of viscous drops, Prosperetti [8] predicted the same effect. We also find that for small-amplitude ($a/b=1.2$) oscillations, the response for both $\mathrm{Re}=1$ and 0.5 is a slow overdamped aperiodic return to the circular shape, while aperiodic critical damping was seen to occur at a slightly higher $\mathrm{Re}(\approx 1.1)$. Note that for globular drops, Basaran [14] and Meradji *et al.* [17] predicted a transition from underdamped periodic oscillations to an aperiodic decay mode for $1.3<\mathrm{Re}<1.4$ and $1.2<\mathrm{Re}<1.4$, respectively, when the drop is released from a second-harmonic shape with initial $a/b \approx 1.015$.

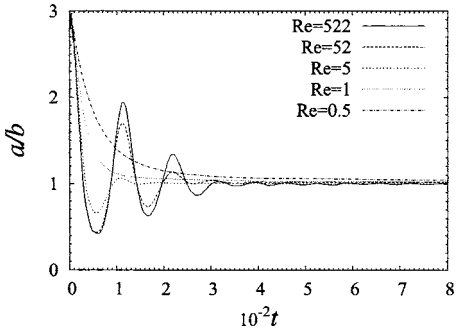

FIG. 10. Effects of Reynolds number on large-amplitude oscillations when the drop is released from an elliptic deformation with $a/b=3$. A transition from periodic to aperiodic wave decay occurs at $\mathrm{Re}=1$. The time is given in reduced units.

The percentage change in frequency during the first period of oscillation as a function of the initial aspect ratio is displayed in Fig. 11 for $\mathrm{Re} \approx 6.27$, ≈ 31.35, and ≈ 62.69. The curves are compared with the experimental results of Trinh and Wang [23]. Also shown are the trends predicted by perturbation analyses [9] and previous axisymmetric calculations of inviscid and viscous fluctuating globular drops [13,14]. The frequency change is measured relative to the Rayleigh $n=2$ frequency given by Eq. (2), which applies to infinitesimal-amplitude oscillations of planar, inviscid drops. The relative change in frequency decreases with increasing aspect ratio for all $\mathrm{Re}>\mathrm{Re}_c$, where Re_c marks the transition from periodic to aperiodic decay. For moderate to large amplitudes, the quadratic decrease of the oscillation frequency with the initial aspect ratio is fairly well reproduced as Re gets large. Compared to the axisymmetric models of Basaran [14], the present two-dimensional calculations predict a relatively faster decrease of the frequency at small initial deformations, especially in drops with low Re, possibly due to the additional dissipative effects of heat conductivity, which were not accounted for in his calculations. At larger deformations, however, the quadratic decrease of the oscillation frequency is fairly well reproduced for $\mathrm{Re} \approx 31.35$ and 62.69.

Finally, Figs. 12 and 13 show the dependence of the decay factor, defined as

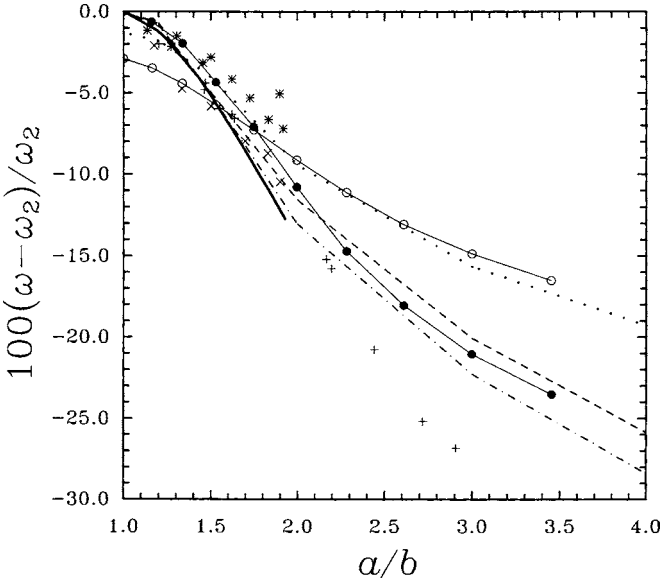

FIG. 11. Percentage change in frequency of the $n=2$ mode during the first period of oscillation as a function of the initial prolate aspect ratio for Re$\approx$6.27 (*dotted line*), $\approx$31.35 (*dashed line*), and $\approx$62.69 (*dot-dashed line*). The results are compared with the experimental results of Trinh and Wang [23] for drops of volume 0.5 cm^3 (*asterisks*) and 1 cm^3 (*crosses*); the asymptotic prediction of Tsamopoulos and Brown [9] (*solid line*); the finite-element calculations of Patzek *et al.* [13] for inviscid drops (*plus signs*); and the finite-element calculations of Basaran [14] for Re=10 (*open circles*) and Re=100 (*filled dots*).

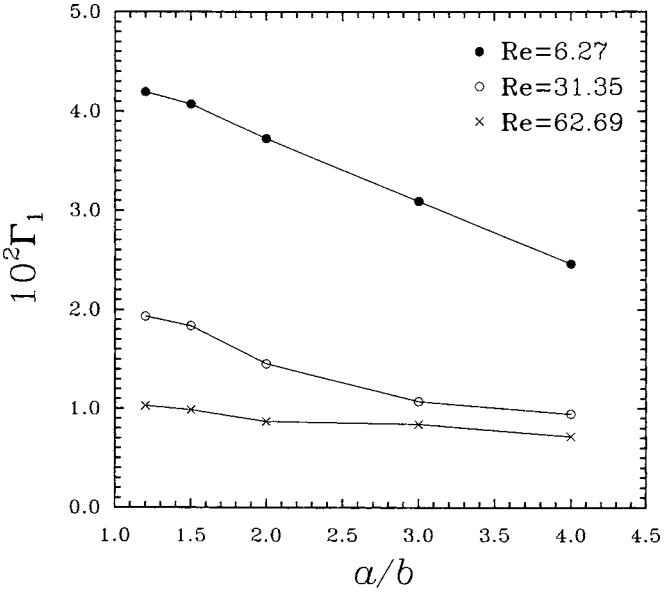

FIG. 12. Decay factor of primary $n=2$ mode during the first period of oscillation as a function of the initial prolate aspect ratio for various Reynolds numbers.

$$\Gamma_i = \frac{1}{\tau_i}\ln\left(\frac{(a/b)_{\tau_{i-1}}-1}{(a/b)_{\tau_i}-1}\right) \quad (i=1,2,\ldots), \tag{31}$$

with the initial aspect ratio and the Reynolds number, respectively. In Eq. (31), the subscript i denotes the period number and the plots in Figs. 12 and 13 refer to the decay factor during the first period of oscillation when $i=1$. For convenience, Γ_1 is multiplied by 100 because the evolutionary time t, rather than t/t_c, has been used to evaluate the period τ_1 in Eq. (31). We see from Fig. 12 that the decay factor during the first period of oscillation decreases with increasing a/b. The decrease in frequency is more pronounced at lower Re. However, as the Reynolds number increases, the decay factor becomes fairly insensitive to the initial disturbance amplitude. This behavior contrasts with the results of Basaran [14], who found that the decay factor increases with increasing aspect ratio. This discrepancy can be understood in terms of the increasing dissipative effects of heat conduction for small-amplitude oscillations. In particular, the effects of heat conduction were tested here on small- and large-amplitude oscillations by varying the coefficient of heat conductivity from $\kappa=1$ (Pe$\approx$0.147) to 10 (Pe$\approx$0.015) at Re$\approx$62.69. For small initial deformations ($a/b=1.5$), the prolate elongation at the end of the first period decreases as long as κ is increased, implying that higher conductivity leads to less elongated shapes. In particular, for $\kappa\leqslant 3$ (i.e., Pe$\gtrsim$0.049) the oscillations are strongly damped over a few periods, while for $\kappa\geqslant 5$ (Pe$\lesssim$0.029), starting from the second period, the oscillations decay very slowly, taking more than about 14 periods to get damped out. Conversely, when the initial aspect ratio is increased to $a/b=3$, the difference in the elongated shapes at the end of the first period are much less pronounced and the oscillation pattern becomes insensitive to variations in κ. Thus, for large-amplitude oscillations the dynamics is primarily governed by the interplay between viscous and inertial forces, while for small amplitudes dissipation is dominated by the combined effects of viscosity and heat conduction.

The dependence of Γ_1 with Re is depicted in Fig. 13 for $a/b=1.5$ and 3. When Re is varied from $\sim$5 to $\sim$50 the

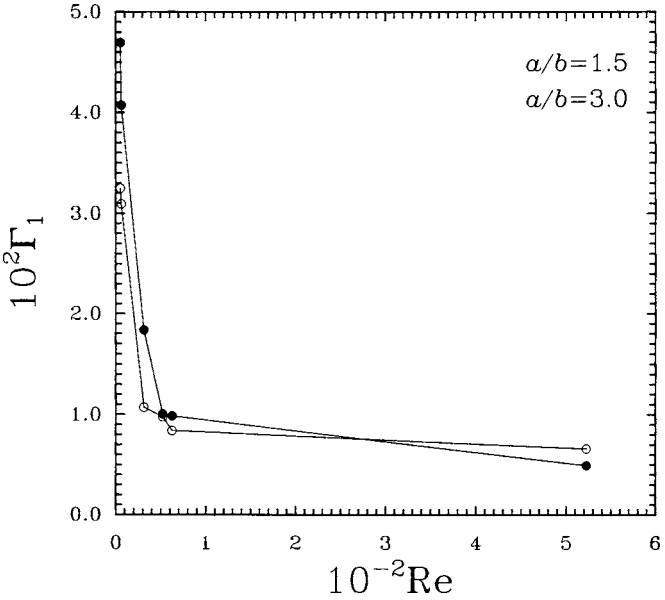

FIG. 13. Decay factor of primary $n=2$ mode during the first period of oscillation as a function of the Reynolds number for drops released from an initial elliptic deformation with $a/b=1.5$ and 3.

decay factor drops from about 5×10^{-2} to approximately 1×10^{-2} for $a/b=1.5$ and only from about 3×10^{-2} to $\sim1\times10^{-2}$ when $a/b=3$. For $\mathrm{Re}\gtrsim50$, it becomes almost insensitive to variations in the Reynolds number. This explains why drop oscillations at moderate and large Re take longer to get damped out, regardless of the initial deformation.

V. CONCLUSIONS

In this paper we have used standard smoothed particle hydrodynamics (SPH), coupled with an adaptive density kernel estimation procedure [30], to investigate the nonlinear oscillations of heat-conductive, viscous, planar drops that are released from a static elliptic deformation in a vacuum surrounding with zero gravity. Three dimensionless parameters govern the nonlinear oscillations: the Reynolds number (Re), the Péclet number (Pe), and the initial prolate aspect ratio (a/b). Attention here has been focused on small- to large-amplitude oscillations ($1.2\leqslant a/b\leqslant4$) for $0.5\lesssim\mathrm{Re}\lesssim522$ and $0.015\lesssim\mathrm{Pe}\lesssim0.15$, respectively.

The numerical results show that for small-amplitude oscillations ($a/b\leqslant2$) damping is due to the combined effects of viscous dissipation and heat conduction, while for large-amplitude oscillations ($a/b\geqslant3$) the action of viscous dissipation and surface tension forces govern the motion. The drop shape evolutions for ($a/b\geqslant3$) and $\mathrm{Re}\gtrsim60$ strongly resemble those for axisymmetric drops that are released from a prolate spheroidal shape [14,17] and those reported from microgravity experiments of fluctuating water drops on board the Space Shuttle Columbia [27]. Modal decomposition of the oscillations show that the amplitude of the primary $n=2$ mode dominates the motion, while the presence of higher harmonics is due to nonlinear coupling with the primary mode, in accordance with predictions from perturbation analyses [9].

The calculations also show that for large-amplitude oscillations, the transition from periodic to aperiodic decay occurs at $\mathrm{Re}=1$, while for small amplitudes ($a/b=1.2$) the transition occurs at $\mathrm{Re}\approx1.1$, in agreement with the trends established by previous finite-element calculations [14,17]. The quadratic decrease of the frequency for moderate and large initial deformations at large Re is also reproduced. We find that in general the decay factor increases with decreasing Re and becomes fairly insensitive to the initial deformation for $\mathrm{Re}\gtrsim50$. Moreover, the effects of heat conduction causes an increase of the decay factor with decreasing initial aspect ratio in contrast with previous findings that indicate the converse for oscillating viscous drops with no heat conduction [14].

In future papers, we will consider extensions and refinements of the present method to calculate the nonlinear oscillations of both fully three-dimensional globular drops and the evolution of long liquid filaments. In particular, the inclusion of an anisotropic smoothing kernel along with the adaptive kernel estimation procedure will result in a substantial increase in the resolving power of the SPH method for the same total number of particles, without any corresponding increase in computational run time.

ACKNOWLEDGMENTS

This work was financially supported by the Instituto Venezolano de Investigaciones Científicas (IVIC).

[1] Lord Rayleigh, Proc. R. Soc. London **29**, 71 (1879).
[2] Lord Kelvin, in *Mathematical Papers* (Clay & Sons, London, 1890), Vol. 3, p. 384.
[3] H. Lamb, *Hydrodynamics* (Cambridge University Press, Cambridge, England, 1932).
[4] S. Chandrasekhar, Proc. London Math. Soc. **9**, 141 (1959).
[5] W. H. Reid, Q. Appl. Math. **18**, 86 (1960).
[6] C. A. Miller and L. E. Scriven, J. Fluid Mech. **32**, 417 (1968).
[7] P. L. Marston, J. Acoust. Soc. Am. **67**, 15 (1980).
[8] A. Prosperetti, J. Fluid Mech. **100**, 333 (1980).
[9] J. A. Tsamopoulos and R. A. Brown, J. Fluid Mech. **127**, 519 (1983).
[10] G. B. Foote, J. Comput. Phys. **11**, 507 (1973).
[11] C. T. Alonso, in *Proceedings of the International Colloquium on Drops and Bubbles*, edited by D. J. Collins, M. S. Plesset, and M. M. Saffren, Jet Propulsion Laboratory, 1974, p. 139.
[12] T. S. Lundgren and N. N. Mansour, J. Fluid Mech. **194**, 479 (1988).
[13] T. W. Patzek, R. E. Benner Jr., O. A. Basaran, and L. E. Scriven, J. Comput. Phys. **97**, 489 (1991).
[14] O. A. Basaran, J. Fluid Mech. **241**, 169 (1992).
[15] E. Becker, W. J. Hiller, and T. A. Kowalewski, J. Fluid Mech. **258**, 191 (1994).
[16] F. Mashayek and N. Ashgriz, Phys. Fluids **10**, 1071 (1998).
[17] S. Meradji, T. P. Lyubimova, D. V. Lyubimov, and B. Roux, Cryst. Res. Technol. **36**, 729 (2001).
[18] T. W. Patzek, O. A. Basaran, R. E. Benner, and L. E. Scriven, J. Comput. Phys. **116**, 3 (1995).
[19] R. M. S. M. Schulkes, J. Fluid Mech. **309**, 277 (1996).
[20] P. K. Notz and O. A. Basaran, J. Fluid Mech. **512**, 223 (2004).
[21] P. Marston and R. Apfel, J. Colloid Interface Sci. **68**, 280 (1979).
[22] D. M. Herlach, R. F. Cochrane, I. Egry, H. J. Fecht, and A. L. Greer, Int. Mater. Rev. **38**, 273 (1993).
[23] E. Trinh and T. G. Wang, J. Fluid Mech. **122**, 315 (1982).
[24] E. Becker, W. J. Hiller, and T. A. Kowalewski, J. Fluid Mech. **231**, 189 (1991).
[25] M. Popoular and C. Parayre, Phys. Rev. Lett. **78**, 2120 (1997).
[26] T. G. Wang, A. V. Anilkumar, and C. P. Lee, J. Fluid Mech. **308**, 1 (1996).

[27] R. E. Apfel, Y. Tian, J. Jankovsky, T. Shi, X. Chen, R. G. Holt, E. Trinh, A. Croonquist, K. C. Thornton, A. Sacco, Jr., C. Coleman, F. W. Leslie, and D. H. Matthiesen, Phys. Rev. Lett. **78**, 1912 (1997).
[28] S. Nugent and H. A. Posch, Phys. Rev. E **62**, 4968 (2000).
[29] A. Tartakovsky and P. Meakin, Phys. Rev. E **72**, 026301-1 (2005).
[30] B. W. Silverman, *Density Estimation for Statistics and Data Analysis* (Chapman & Hall, London, England, 1996).
[31] L. Di G. Sigalotti, J. Klapp, E. Sira, Y. Meleán, and A. Hasmy, J. Comput. Phys. **191**, 622 (2003).
[32] L. Di G. Sigalotti, H. López, A. Donoso, E. Sira, and J. Klapp, J. Comput. Phys. **212**, 124 (2006).
[33] J. Bonet and T.-S. L. Lok, Comput. Methods Appl. Mech. Eng. **180**, 97 (1999).
[34] J. P. Morris, P. J. Fox, and Y. Zhu, J. Comput. Phys. **136**, 214 (1997).
[35] L. D. Landau and E. M. Lifshitz, *Fluid Mechanics* (Pergamon, Oxford, England, 1987).
[36] L. Di G. Sigalotti and H. López, Comput. Math. Appl. (to be published).
[37] L. B. Lucy, Astron. J. **83**, 1013 (1977).
[38] J. P. Morris, Int. J. Numer. Methods Fluids **33**, 333 (2000).
[39] R. J. Twiss and E. M. Moores, *Structural Geology* (Freeman, New York, 1992).
[40] P. R. Shapiro, H. Martel, J. V. Villumsen, and J. M. Owen, Astrophys. J., Suppl. Ser. **103**, 269 (1996).